# Three-Dimensional Atomic Structure of Metastable Nanoclusters in Doped Semiconductors

Martin Couillard,[1,*] Guillaume Radtke,[2] Andrew P. Knights,[3] and Gianluigi A. Botton[4]

[1]*Brockhouse Institute of Materials Research and Canadian Centre for Electron Microscopy, McMaster University,
1280 Main Street West, Hamilton, Ontario L8S 4L7, Canada*
[2]*IM2NP UMR 6242 CNRS, Faculté des Sciences de Saint-Jérôme, case 262,
Université Paul Cézanne-Aix Marseille III, 13397 Marseille cedex 20, France*
[3]*Department of Engineering Physics, McMaster University, 1280 Main Street West, Hamilton, Ontario L8S 4L7, Canada*
[4]*Department of Materials Science and Engineering and Canadian Centre for Electron Microscopy, McMaster University,
1280 Main Street West, Hamilton, Ontario L8S 4L7, Canada*
(Received 28 June 2011; published 28 October 2011)

Aberration-corrected scanning transmission electron microscopy is used to determine the atomic structure of nanoclusters of cerium dopant atoms embedded in silicon. By channeling electrons along two crystallographic orientations, we identify a characteristic zinc-blende chemical ordering within CeSi clusters coherent with the silicon host matrix. Strain energy limits the size of these ordered arrangements to just above 1 nm. With the local order identified, we then determine the atomic configuration of an individual subnanometer cluster by quantifying the scattering intensity under weak channeling condition in terms of the number of atoms. Analysis based on single-atom visualization also evidences the presence of split-vacancy impurity complexes, which supports the hypothesis of a vacancy-assisted formation of these metastable CeSi nanophases.

In the early stages of clustering in doped crystalline materials, preceding the formation of larger thermodynamically stable precipitates, the location of solute atoms within the solvent lattice is heavily constrained by interfacial, strain, and electronic energies [1]. In this out-of-equilibrium context, unexpected metastable chemical phases may be stabilized [2,3]. Determining the atomic configuration of such phases, which may appear in clusters of dimension below 2 nm, presents a challenge. The small interacting volume limits the use of x-ray or electron diffraction techniques, while structural inhomogeneities complicate the interpretation of signals averaged over mixed populations of isolated and clustered impurities, such as in Rutherford backscattering, emission channeling, positron annihilation, or extended x-ray absorption fine structure experiments. Hence, an unambiguous description of possible metastable phases in dopant nanoclusters necessitates a 3D real-space analysis.

In this Letter, we elucidate the atomic structure of individual embedded subnanometer clusters coherent with a crystalline matrix using annular dark-field (ADF) imaging in aberration-corrected scanning transmission electron microscopy (STEM). Our work focuses on the model system of silicon doped with cerium, a reactive rare-earth metal with multiple silicide phases and two possible oxidation states ($3^+$, $4^+$). ADF-STEM imaging provides a contrast related to the atomic number [4] that can reach single-atom sensitivity [5–8]. With the recent advent of aberration-corrected electron optics [9,10], the visibility of single dopant atoms has considerably increased [11–16], and the chemical sensitivity has reached the atomic number level

[17]. Considerable efforts have been directed toward the development of 3D imaging techniques based on electron tomography [18], on focal series reconstruction (exploiting the reduced depth of focus in aberration-corrected instruments) [19], or more recently on a statistical analysis of scattering intensities combined with discrete tomography [11]. However, these approaches require the acquisition of multiple images, and are therefore not ideally suited to the study of beam-sensitive objects, such as metastable nanophases. Here, in a two step analysis, we provide 3D information by first imaging in strong channeling (on-axis) conditions along distinct crystallographic zone axes, and then by quantifying the ADF-STEM signal in terms of number of dopant atoms for images taken under weak channeling (off-axis) conditions. From on-axis images, we identify a characteristic zinc-blende ordering, while from a single off-axis image we determine the structure of an individual cluster with atomic sensitivity.

A widely used approach to incorporate dopant atoms in semiconductors is ion implantation. Following ion bombardment, a thermal annealing step is required to heal impact damage. To understand dopant migration and clustering during this process, we present maps of individual cerium atoms, acquired both before [Fig. 1(a)] and after [Fig. 1(b)] a thermal annealing process. Imaging was performed in a FEI-Titan 80-300 STEM operated at 200 keV, and equipped with two aberration correctors. The specimens were prepared by tripod polishing combined with a brief (10 min) low voltage ($< 500$ V) ion milling. Only thin ($\lesssim 10$ nm) specimen regions were analyzed in order to avoid strong channeling effects. The convergence
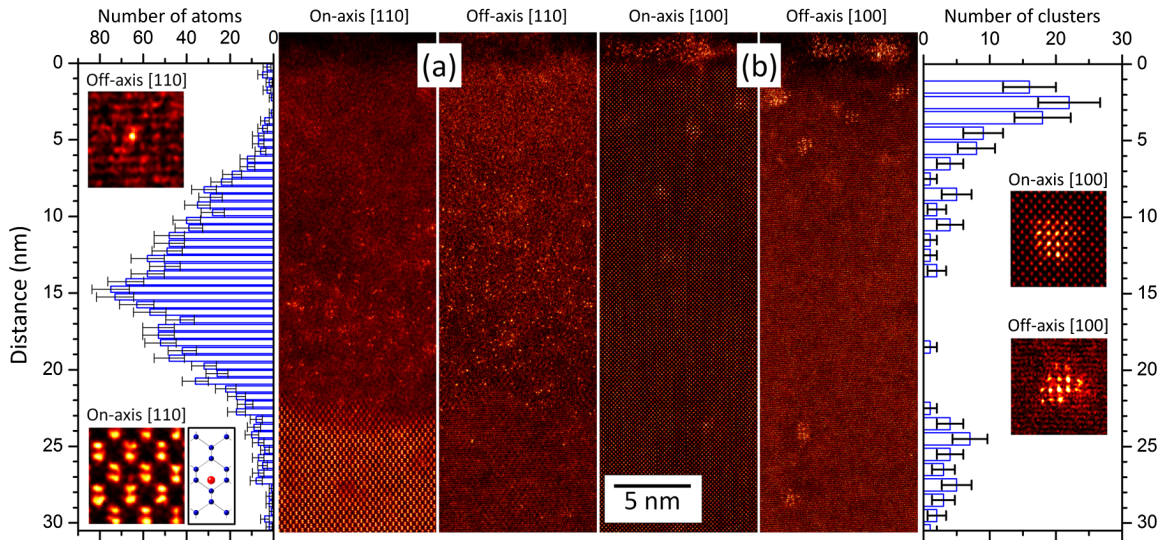
FIG. 1 (color online).   ADF-STEM images of Ce dopant atoms implanted in Si(100) taken (a) before and (b) after a thermal annealing process. In (a), the image on the left was taken along the [110] zone axis, and the image on the right was taken with a 4° tilt from [110]. The depth distribution of dopant atoms is shown on the left and includes insets showing individual dopant atoms in the crystalline silicon region from an off-axis (top) and on-axis (bottom) image. The dimension of inset images is 1.2 nm. A sphere representation of a tetrahedral interstitial atom is also shown in the bottom inset. In (b), the image on the left was taken along the [100] zone axis, and the image on the right was taken with a 4° tilt from [100]. The depth distribution of dopant clusters is shown on the right and includes insets showing an on-axis (top) and off-axis (bottom) image. The dimension of inset images is 2.5 nm. Inset images have been low-pass Fourier filtered (Butterworth) using parameters that ensured no significant broadening of a 0.8 Å Gaussian function. All images are displayed on a nonlinear intensity scale.

semiangle was set to 24 mrad for on-axis images, 18 mrad for off-axis images, and the ADF inner semiangle was set to 60 mrad.

Following the implantation process ($3 \times 10^{14}$ Ce ions/cm$^2$ implanted at 20 keV, and at an angle of 7° to the surface normal), two regions in the silicon substrate can be identified [Fig. 1(a)]: a 22 nm layer at the surface, amorphized by ion impacts, and a deeper crystalline region (albeit with subamorphizing threshold ion induced damage). Most of the cerium dopant penetrate <20 nm in depth and are located in the amorphous silicon ($a$-Si) layer. Some dopants are also detected in the crystalline silicon ($c$-Si) region, primarily occupying interstitial sites (bottom inset). The visibility of dopant atoms in $c$-Si is enhanced by tilting the specimen 4° away from the [110] zone axis (top inset). To ensure that dopant position along the TEM optical axis did not strongly affect the ADF intensity, the convergence semiangle was lowered to 18 mrad, giving a depth of focus $\sim 2\lambda/\alpha^2 \sim 15$ nm (where $\lambda$ is the electron wavelength and $\alpha$ is the convergence semiangle) larger than the specimen thickness. A depth distribution, shown on the left, can then be obtained by directly counting atoms in off-axis images.

During the annealing process (5 min in flowing N$_2$ at 700 °C), the amorphized silicon recrystallizes, and the cerium impurities migrate [Fig. 1(b)]. A large fraction of cerium atoms has been pushed out of the matrix and have formed clusters in the native oxide at the surface (estimated to be 2 nm in thickness). Inside the silicon lattice, isolated

impurity atoms remain while sub-nm clusters have also formed. From off-axis images, with enhanced dopant visibility (inset), we extract a depth distribution of clusters embedded in silicon. Whereas the dopant profile after implantation shows a single maximum, the cluster profile following annealing reaches two maxima at different depths. A majority of clusters is found a few nanometers underneath the surface and is associated with the large amount of impurities pushed by the recrystallization front. The presence of a second distribution centered at about 25 nm in depth might arise from the fraction of impurities already present in the $c$-Si after implantation and therefore not affected by the strong segregation associated with the recrystallization process. In both regions of this bimodal distribution, a majority of clusters are found to display the same characteristic chemical ordering.

Typical ordered clusters observed along the [110] and [100] zone axis are displayed in Figs. 2(a) and 2(b), respectively, with their corresponding atomic models in 2(c) and 2(d). The observed Ce atoms occupy substitutional sites, and a pattern coherent with the Si lattice emerges for both crystallographic orientations. Along [100], Ce dopants organize into squares with a side length corresponding to half the Si lattice parameter; along [110], they form isosceles triangles by occupying only one of the silicon dumbbell positions. These two patterns reveal a zinc-blende (B3) lattice, which consists of two interpenetrating fcc sublattices, respectively, built from Ce and Si atoms, and shifted with respect to each other by
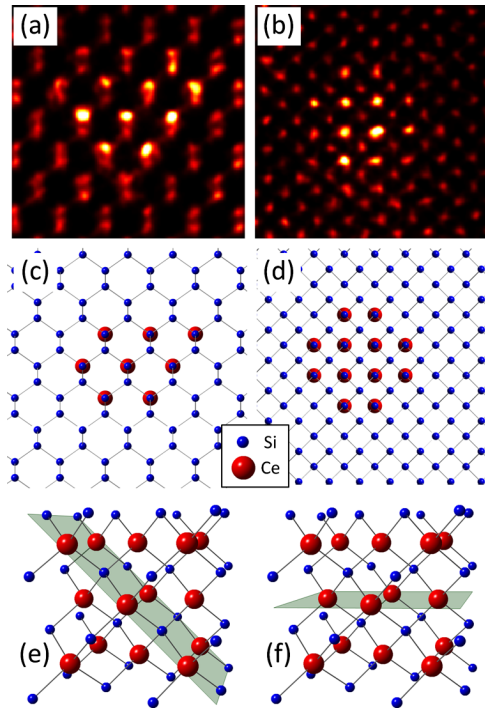
FIG. 2 (color online).   ADF-STEM images of clusters taken along the (a) [110] and (b) [100] zone axes, with their corresponding atomic models in (c) and (d). The images were taken from two different TEM specimens, have been low-pass filtered, and are displayed on a nonlinear intensity scale. Their dimension is 2 nm. Panels (e) and (f) display the (110) and (100) planes in a zinc-blende lattice.

$(a/4, a/4, a/4)$, where $a$ is the cubic lattice parameter. The triangle and square patterns observed experimentally correspond to projections of the zinc-blende lattice onto the (110) and (100) planes shown in Figs. 2(e) and 2(f). This atomic arrangement represents an efficient way to maintain the overall symmetry of the Si matrix lattice structure and therefore the coherence of the matrix-cluster interface while allowing the local segregation of a large amount of Ce atoms.

Our proposed B3-type structure is not listed in the known equilibrium phases of bulk cerium silicides [20]. Instead, it appears to be a metastable phase for sub-nm CeSi clusters embedded in a crystalline Si matrix, where interfacial energy stabilizes the ordered atomic arrangement, while strain energy, related to the much larger atomic radius of Ce ($\sim 1.85$ Å) with respect to Si ($\sim 1.10$ Å) [21], limits its size to about 1 nm ($\sim 80$ Ce atoms). This local ordering also maintains a tetrahedral environment for both Si and Ce atoms, consistent with the formation of four $\sigma$ Ce-Si covalent bonds. Indeed, in tetrahedral coordination and due to their proximity in energy, four $sd^3$ hybrids can be built from extended Ce-$6s$ and crystal-field split $5d$ orbitals of $T_2$ symmetry. As noted by Pauling [22], an admixture of antisymmetric $6p$ or $4f$ states to these centrosymmetric $sd^3$ hybrids would produce directed orbitals

truly pointing toward the nearest-neighbor Si atoms. A $\sigma$ overlap can then occur between each of these Ce hybrids and their Si-$sp^3$ counterparts. Owing to its atomic electronic configuration [Xe]$4f^1 5d^1 6s^2$, the four Ce valence electrons can pair with the Si valence electrons on the resulting bonding orbitals, leading to an electronic contribution to the stabilization of this particular phase.

Recurring deviations from the perfectly ordered structure were also observed. A typical example for [100] images is shown in Fig. 3, where some of the Ce atoms are displaced halfway toward the next silicon lattice site. Although this atomic arrangement along the [100] zone axis is compatible with the presence of Ce atoms in a hexagonal interstitial site, the large strain associated with this configuration would make the observed self-organized structures unlikely. The high density of vacancies created during ion implantation, possessing potential for complexing into higher order defects upon annealing, supports the alternative model of a split-vacancy impurity complex [inset in Fig. 3(b)], already deduced in similar systems [23], and often expected for oversized impurities [24]. The direct imaging of Ce atoms on such bond-centered sites at the edges of forming nanoclusters is consistent with the notion of a vacancy-assisted clustering process. Vacancies present during recrystallization are indeed essential to the rapid diffusion of substitutional Ce, leading eventually to the formation of the observed CeSi nanophase.

After having established the local B3 ordering within the nanophase, it is possible to determine in a second step the 3D atomic structure of an individual CeSi cluster by quantifying the ADF intensity in terms of number of atoms. For increased accuracy in the analysis, we image along a direction slightly off a major zone axis in order to avoid channeling effects due to the Si matrix and to increase the visibility of the dopant atoms. The off-axis image in Fig. 4(a), acquired near the [100] orientation, shows a cluster with its typical square pattern corresponding solely to the visualization of the Ce fcc sublattice standing above a uniform background due to the Si matrix. For clarity,
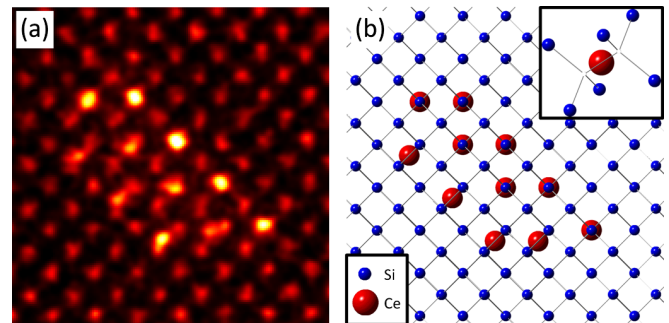


FIG. 3 (color online).   (a) ADF-STEM image (low-pass filtered and on a nonlinear intensity scale, dimension of 2 nm) taken along the [100] zone axis of a CeSi cluster, with the corresponding atomic model shown in (b). A sketch of a Ce-split-vacancy configuration is presented as an inset in (b).
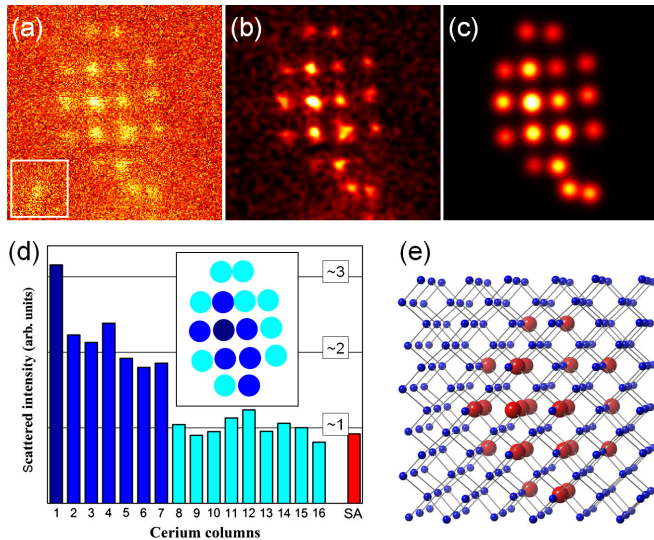
FIG. 4 (color online). (a) ADF-STEM image of a CeSi cluster taken along a direction close to the [100] zone axis (not filtered and displayed on a linear intensity scale). (b) Low-pass filtered image. The specimen was tilted 6° along the (001) tilt axis, and then 4° along the orthogonal axis. The convergence semiangle is 18 mrad, and the sampling is 0.009 nm/pixel. The inset in (a) shows an individual atom. (c) Model of the image shown in (a) obtained following the procedure described in Ref. [25], with (d) the graph of integrated intensity for each Ce column in the cluster and for the single atom (SA) shown in (a). The inset presents a model of the cluster with an estimation of the number of atoms in each column. (e) Sphere representation of the cluster.

Fig. 4(b) shows the same image after low-pass filtering. The sampling was increased to more than 10 pixels/Å, and the convergence angle was lowered to 18 mrad to increase the depth of field.

For a proper extraction of the Ce column intensities, an expectation model of the experimental image has been built and optimized following the procedure described in Ref. [25]. The refined model of Fig. 4(a) is shown in 4(c), along with a graph in 4(d) of the corresponding scattering intensities extracted as the volume under the optimized 2D Gaussians. The graph also includes the integrated intensity obtained for a single reference atom [labeled SA, and shown as an inset in 4(a)]. From the steplike variations in intensity, the number of Ce atoms in each column of the cluster is estimated, as shown in the inset of Fig. 4(d), giving a total for the whole cluster of ∼24 atoms. Even if the exact depth positioning of the Ce atoms with respect to each other cannot be assessed, only a finite number of combinations coherent with the zinc-blende CeSi structure remain, and the 3D nature of the cluster is revealed. A sphere representation compatible with the observed cluster is shown in Fig. 4(e).

To summarize, a two-step, generally applicable approach based on high-resolution ADF-STEM imaging has been developed to determine the local chemical order of nanoclusters embedded in a crystalline matrix and to retrieve their three-dimensional atomic structure. Using the system of Ce impurities in silicon, we have evidenced the presence of a zinc-blende metastable phase for CeSi sub-nm clusters that is absent from the bulk cerium silicide phase diagram. Even if limited to dopant atoms of higher atomic number than substrate atoms, our method based on weak channeling has demonstrated an increased atomic sensitivity. Further, it is well suited for beam-sensitive systems and could potentially be applied to resolve more complex structures, such as nanoclusters consisting of multiple elements or embedded in compound semiconductors. Quantitative information extracted this way has the potential to provide insights into the physics of out-of-equilibrium atomic processes leading to the formation of structures stable only on the scale of a few nanometers.

*Current address: National Research Council Canada, 1200 Montreal Road, Ottawa, Ontario K1A 0R6, Canada.
martin.couillard@nrc.ca

[1] P. M. Fahey *et al.*, Rev. Mod. Phys. **61**, 289 (1989).
[2] M. Seibt *et al.*, Phys. Status Solidi A **171**, 301 (1999).
[3] F. H. Baumann and W. Schröter, Phys. Rev. B **43**, 6510 (1991).
[4] S. J. Pennycook and D. E. Jesson, Phys. Rev. Lett. **64**, 938 (1990).
[5] A. V. Crewe *et al.*, Science **168**, 1338 (1970).
[6] P. D. Nellist and S. J. Pennycook, Science **274**, 413 (1996).
[7] P. M. Voyles *et al.*, Nature (London) **416**, 826 (2002).
[8] U. Kaiser *et al.*, Nature Mater. **1**, 102 (2002).
[9] D. A. Muller, Nature Mater. **8**, 263 (2009).
[10] M. Haider, Nature (London) **392**, 768 (1998).
[11] S. Van Aert *et al.*, Nature (London) **470**, 374 (2011).
[12] H. Okuno *et al.*, Appl. Phys. Lett. **96**, 251908 (2010).
[13] N. Shibata *et al.*, Nature Mater. **8**, 654 (2009).
[14] V. Ortalan *et al.*, Nature Nanotech. **5**, 843 (2010).
[15] S. H. Oh *et al.*, Nano Lett. **8**, 1016 (2008).
[16] Y. Oshima *et al.*, Phys. Rev. B **81**, 035317 (2010).
[17] O. L. Krivanek *et al.*, Nature (London) **464**, 571 (2010).
[18] I. Arslan *et al.*, Science **309**, 2195 (2005).
[19] H. L. Xin and D. A. Muller, Microsc. Microanal. **16**, 445 (2010).
[20] M. V. Bulanova *et al.*, J. Alloys Compd. **345**, 110 (2002).
[21] J. C. Slater, J. Chem. Phys. **41**, 3199 (1964).
[22] L. Pauling, J. Am. Chem. Soc. **53**, 1367 (1931).
[23] S. Decoster *et al.*, Appl. Phys. Lett. **93**, 141907 (2008).
[24] H. Höhler *et al.*, Phys. Rev. B **71**, 035212 (2005).
[25] S. Van Aert *et al.*, Ultramicroscopy **109**, 1236 (2009).